J. Fluid Mech. (2006), *vol.* 559, *pp.* 57–80.
doi:10.1017/S0022112006009979 Printed in the United Kingdom

Topographically controlled, breaking-wave-induced macrovortices. Part 2. Changing geometries

By A. B. KENNEDY[1], M. BROCCHINI[2], L. SOLDINI[3] AND E. GUTIERREZ[1]

[1]Department of Civil & Coastal Engineering, University of Florida, Gainesville, FL 32611-6590, USA
[2]D.I.Am., Università di Genova, 16145 Genova, Italy
[3]Istituto di Idraulica e Infrastrutture Viarie, Università Politecnica delle Marche, 60131 Ancona, Italy

(Received 12 February 2005 and in revised form 22 September 2005)

This is the second part of a series examining the behaviour of breaking-wave-induced macrovortices. The first part examined theoretically general behaviours during startup conditions, and gave computational results for macrovortex generation and their evolution on widely spaced breakwaters. In this paper, we extend and test qualitatively and quantitatively some of the basic results of Part 1, in particular the initial longshore vortex transport for a wide range of geometries ranging from narrow rip current topographies to isolated breakwaters. Accounting for the presence of a shoreline is found to be necessary for the representation of longshore vortex transport. Results show vortex motion ranging from strongly offshore in the case of a narrow rip current, to strongly longshore in the case of an isolated breakwater. Even with the significant approximations inherent in the analytical predictions, numerical computations using time-domain Boussinesq-type equations and laboratory experiments confirm the trends. Part 3 examines the horizontal mixing features of wave-induced flows over isolated (single-breakwater configuration) or multiple (rip-current configuration) submerged structures.

1. Introduction

Whenever the strength of breaking varies along the crest of a wave, velocity circulation along a closed path cutting the wave crest (for simplicity called 'circulation' hereinafter) is generated. In shallow water, this leads to large-scale macrovortices with a vertical axis (Peregrine 1998, 1999; Bühler & Jacobson 2001). Depending on the details of the local bathymetry the behaviour and transport of these macrovortices can be quite different. Peregrine (1999) predicted that for small gaps in breaking, a vortex pair would be generated that, through mutual advection, would be transported offshore. The opposite scenario, short lengths of breaking waves, would produce vortices that were transported shoreward. An option not considered by Peregrine has comparable breaking lengths and gaps, which by itself would produce little net cross-shore vortex transport.

Although differential breaking occurs naturally from variability in wave direction and amplitude, these processes constantly change in space and time. In contrast, topographically controlled wave breaking produces circulation about a stationary location. Such circulation cells occur at submerged breakwaters and on rip current

topographies, and are the subject of this and the companion paper (Part 1). In Part 1 (Brocchini *et al.* 2004), we considered the generation of circulation during startup conditions using several different techniques, and found commonalities. Predictive expressions were derived for the generation of circulation given the geometry and incident wave conditions. Vortex generation and circulation on widely spaced, submerged breakwaters was examined numerically. Good agreement was found between predicted and observed vortex detachment periods.

This paper (Part 2) builds on the results of Part 1 for topographies ranging from isolated breakwaters to narrow rip currents. The factors governing the initial direction of vortex transport are found to be almost entirely dependent on the details of the bar–trough–gap geometry as was predicted in Part 1. However, while Part 1 only considered cross-shore transport, in some cases the proximity of the shoreline means that longshore vortex transport initially dominates. Again, this is largely fixed by the geometry.

Companion paper Part 3 (Piattella, Brocchini & Mancinelli 2006) examines the horizonal mixing features of wave-induced flows over isolated (single-breakwater configuration) or multiple (rip-current configuration) structures.

The remainder of the paper has several distinct portions: § 2 gives an analysis of the important geometrical influences for initial vortex transport and provides predictive relations. Section 3 extends these simplified relations, uses them to predict vortex transport on nearshore topographies ranging from narrow rip currents to widely spaced breakwaters, and compares trajectories with laboratory and numerical tests. Finally, results are discussed and summarized in § 4. The major theme followed throughout all of the sections is that a relatively small number of processes provide reasonable predictions of the overall modes of behaviour, even after some rather drastic simplifications.

2. Macrovortex transport at startup

For large-scale, wave-forced nearshore circulation (such as rip current cells) with typical length scale L_0, depth scale h_0, and large-scale rotational fluid velocity U_0, vortical time scales are generally longer than irrotational time scales. This is because free irrotational motions travel with the long-wave speed proportional to $t^*_{irr} = t\sqrt{gh_0}/L_0$, while vorticity is transported at the fluid speed and so $t^*_{rot} = tU_0/L_0$. Thus, the ratio of rotational to irrotational dimensionless time varies with the large-scale Froude number $t^*_{rot}/t^*_{irr} = Fr \equiv U_0/\sqrt{gh_0}$. The circulations with which we are concerned are almost always found to have a large-scale Froude number $Fr \ll 1$ and, thus, much longer characteristic time scales than the irrotational motions. Because of this difference in time scales, and because irrotational motions have much smaller net transport over a cycle than rotational motions (Peregrine 1998), for the most part it is a good approximation to consider only rotational effects on the large-scale fluid transport, except at the very early stages of wave breaking. As in Part 1, we consider macrovortex generation and transport at startup, when pre-existing vorticity and large-scale turbulent fluctuations are much smaller than in fully developed turbulent circulation at later times.

Figure 1 is a schematic of the major processes which influence the transport of macrovortex [1], which is generated at the transition between strong breaking on the bar or breakwater, and weak or no breaking in the deeper gap. Processes may be divided into three groups: general breaking wave and surface elevation influence [0]; mutual advection between vortex [1] and other vortices [2–4]; and self-advection

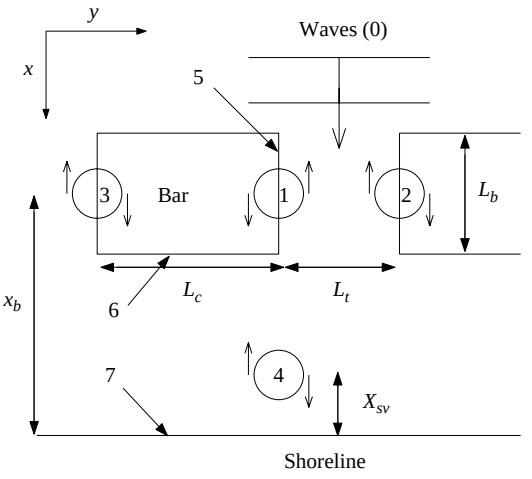

FIGURE 1. Definition sketch for macrovortex transport. [0] Incident waves; [1] main bar vortex under consideration; [2] vortex across the gap with opposite circulation; [3] vortex along the bar with opposite circulation; [4] shore vortex with opposite circulation; [5] side slope of bar or breakwater; [6] back slope of bar or breakwater; [7] shoreline.

of vortex [1] on a varying topography [5–7]. As geometries change, the relative importance of each component varies.

The three groups of processes also serve well to define the four different stages of macrovortex transport given in Part 1. During stage (i), all processes are active, but a general shoreward motion from breaking waves [0] is by far the strongest. In stage (ii), gradients in mean water levels are in approximate balance with the irrotational portion of breaking wave forcing: here mutual advection [2–4] and self-advection [5–7] dominate. During stage (iii), vortices leave the side slopes of the breakwater and are dominated by mutual advection [2–4] and by self-advection with the sloping shoreline [7]. During stage (iv) conditions consecutively generated vortices, bottom friction, and possibly depth-varying effects and wave–current interaction become important as they define the overall circulation cells and limit their strength. The remainder of this section develops relations for vortex transport based on processes [0–7], and examines their strengths and relationship to geometrical parameters. Based on this, simplified relations are proposed. We concentrates on stages (ii)–(iii), when mutual and self advection dominate, and dissipative effects and changes in effective geometry caused by large-scale vorticity transport have not yet become dominant. However, in § 3, comparison with laboratory experiments and numerical tests shows that these simple relations can provide surprisingly good predictions well past the point where they are strictly valid.

2.1. *Shoreline influence on mutual advection*

A shallow-water point vortex with circulation $\Gamma \equiv \oint \boldsymbol{U} \cdot \mathrm{d}l$ on a constant-depth, infinite domain induces a velocity

$$U_\theta = \frac{\Gamma}{2\pi r} \tag{2.1}$$

at any point throughout the domain, where U_θ is the velocity orthogonal to the radius r in a right-hand sense, and $r > 0$ is the distance from the vortex core. Thus, the separation distance between two vortices with known strengths can be used to find the mutual advection induced by these vortices.

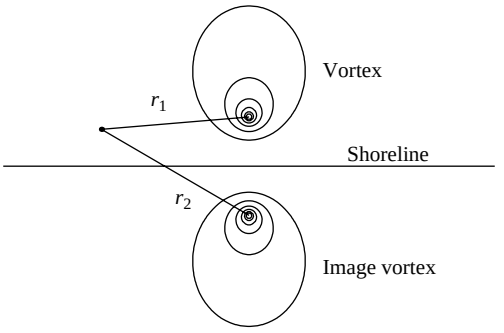

FIGURE 2. Streamlines for a point vortex on a planar beach.

However, when the distance to the shoreline, x_b, is small relative to the separation distance between the vortices, r, (2.1) loses accuracy. This situation becomes important when either the crest length L_c or gap width L_t is comparable to or greater than the shoreline distance x_b.

A streamfunction for a point vortex that includes the effects of the shoreline on a planar beach is given, based on that in Lamb (1932), as

$$\psi = -\frac{s\Gamma}{2\pi}(r_1 + r_2)[K(m) - E(m)] \tag{2.2}$$

where

$$u = -\frac{1}{d}\frac{\partial \psi}{\partial y}, \quad v = \frac{1}{d}\frac{\partial \psi}{\partial x}, \tag{2.3}$$

s is the planar beach slope, d is the local depth, r_1 and r_2 are the distances between the point considered and either the vortex core or its image. $K(m)$ and $E(m)$ are complete elliptic integrals in terms of the parameter, m, not the modulus k (Abramowitz & Stegun 1964), and

$$m = \left(\frac{r_2 - r_1}{r_2 + r_1}\right)^2 \quad \text{with} \quad m = k^2. \tag{2.4}$$

This differs in presentation from Lamb, who implicitly gave results in terms of the modulus k. Figure 2 is a schematic showing the geometry and some streamlines demonstrating the departure from the purely circular orbits found for an infinite flat domain.

There are several situations of interest in which velocities defined by (2.1) and (2.2–2.3) differ significantly; these are introduced as they become important and can change the overall scaling of the flow.

2.2. *Review of Part* 1

Because of the strong three-dimensional topography, exact analytical representations of vortex transport processes are intractable; however, even approximate relations can give very useful and illuminating results. For convenience, we repeat some results of Part 1 for cross-shore transport before examining longshore processes in more detail.

For quasi-steady breaking waves, the cross-shore velocity of vortex [1] during stage (ii) was given as

$$U_1 = \Gamma \left\{ \frac{1}{2\pi} \left(\underbrace{\frac{1}{L_c}}_{[3]} - \underbrace{\frac{1}{L_t}}_{[2]} \right) + \underbrace{\frac{s_5}{d} \frac{1}{4\pi} \left[\log\left(\frac{8d}{s_5 R} \right) - \frac{1}{4} \right]}_{[5]} \right\} \tag{2.5}$$

where numbers in underbraces refer to the process defined in figure 1, s_5 is the side slope of the breakwater, and d and R are, respectively, the local depth and core radius of vortex [1]. During stage (iii), the final term arising from the side slope of the bar [5] disappears.

Relations similar in character to this led to results in Part 1 such as the strong shoreward acceleration during stage (i) of virtually all flows, the potential for vortices meandering along the bar slope (e.g. figure 3 of Part 1), and strong offshore flows in narrow rip current gaps.

Part 1 implicitly assumed that the bar was far enough offshore that shoreline effects on the overall cross-shore flow were negligible. For longshore transport, particularly in the case of wide gaps or isolated bars, reefs or breakwaters this is far less acceptable, as interaction with the shoreline can be a major component of transport.

When shoreline effects cannot be neglected, (2.2)–(2.3) must be used. When bar length or gap width is much greater than the shoreline distance, i.e. for $L_t, L_c \gg x_b$, we may use leading-order asymptotic approximations for $m \to 0$ in (2.2) where $K(m) - E(m) = \pi m/4 + O(m^2)$ (Abramowitz & Stegun 1964), which simplifies velocity representations considerably:

$$\psi = -\frac{s\Gamma}{2\pi}(r_1 + r_2)[K(m) - E(m)] \approx -\frac{s\Gamma}{8}(r_1 + r_2)m + O(m^2). \tag{2.6}$$

Here, vortex [2] acts on vortex [1] inducing an offshore velocity of

$$U_{ma2} = \left[-\frac{1}{d}\frac{\partial \psi}{\partial y} \right]_{y=L_t} = -\frac{3\Gamma}{4}\left(\frac{x_b}{L_t} \right)^3 \frac{1}{L_t} \tag{2.7}$$

on vortex [1], while vortex [3] induces on [1] a shoreward velocity similar to (2.7), with L_t replaced by L_c. Both of these are reduced by $O(x_b/L_t)^3$ from the infinite-domain velocity of (2.1). Thus, during stage (iii) conditions when mutual advection is the only significant cross-shore process, transport is very much reduced if longshore length scales are greater than cross-shore length scales. This becomes important when compared to longshore transport.

2.3. *Longshore vortex transport*

Longshore motion of vortex [1] was not considered directly in Part 1. However, in many cases this is not a reasonable assumption. Waves at an angle to the shoreline generate longshore currents which decay on relatively long time scales and may still be strong even during the low points of wave groups. Tidal currents may be significant in some situations. In addition to this, shore vortices ([4] in figure 1) may be generated by differential wave breaking near the shoreline, and tend to mutually advect the corresponding bar-generated vortices away from the bar and towards the gap. For $L_t \to 0$ shore vortices [4] may be weakened by wave refraction (e.g. MacMahan *et al.* 2005), but for L_t/x_b large enough nearshore breaking will induce significant shore vortices (see also § 3 and Appendix A). Finally, self-advection, both by the bar back

slope [6] and/or the sloping shoreline [7] may transport vortices in either longshore direction. Here we consider only the case of small-angle wave incidence and small tidal velocities, thus avoiding the complicating factor of pre-existing longshore currents. This limitation is to be removed in future work.

Advection by the bar back slope [6] tends to move a vortex away from the gap, i.e. towards the middle of the bar, as seen in figure 3 of Part 1. Its form is similar to the cross-shore self-advection considered in Part 1, except that the back slope of the bar s_6 becomes the relevant slope:

$$V_{sa6} = \frac{\Gamma s_6}{4\pi d}\left[\log\left(\frac{8d}{s_6 R}\right) - \frac{1}{4}\right]. \tag{2.8}$$

This is quite approximate as it assumes small, locally planar slopes, which may be questionable if the topography is strongly three-dimensional. Additionally, self-advection by the bar slope vanishes if a vortex moves into the deeper gap, where no bar exists. Thus, by definition, self-advection by the bar back slope can only be significant during stage (ii) conditions: stage (iii) begins once this process ceases to be important.

self-advection of vortex [1] by the sloping shoreline is always active, and tends to move vortices away from the bars into the gap. Its form is similar to that of (2.8) and is given by

$$V_{sa7} = -\frac{\Gamma}{4\pi x_b}\left[\log\left(\frac{8x_b}{R}\right) - \frac{1}{4}\right]. \tag{2.9}$$

This can be quite significant in many cases as shown in the following.

Mutual longshore advection between bar and shoreline vortices tends to move both toward the gap. At leading order the motion of vortex [1] induced by the shore vortex [4] may be estimated from the infinite-domain relations of (2.1) as

$$V_{ma4} = -\frac{\Gamma_{sv}}{2\pi(x_b - x_{sv})} \tag{2.10}$$

where the subscript $_{sv}$ refers to quantities associated with the shore vortex [4]. The circulation around the shore vortex is not necessarily the same as that around the bar vortex although they may be very similar (see Appendix A). If we do make this additional approximation that $\Gamma_{sv} = \Gamma$, then the longshore velocity of vortex [1] may be estimated as

$$\begin{aligned} V_1 &= \frac{\Gamma}{2\pi}\left\{\frac{s_6}{2d}\left[\log\left(\frac{8d}{s_6 R}\right) - \frac{1}{4}\right] - \frac{1}{2x_b}\left[\log\left(\frac{8x_b}{R}\right) - \frac{1}{4}\right] - \frac{1}{(x_b - x_{sv})}\right\} \\ &= \frac{\Gamma}{2\pi}\left\{\frac{1}{2d}\left[s_6 \log\left(\frac{8d}{s_6 R}\right) - s\log\left(\frac{8d}{sR}\right) + \frac{s - s_6}{4}\right] - \frac{1}{(x_b - x_{sv})}\right\} \end{aligned} \tag{2.11}$$

where s_6 is the back slope of the bar corresponding to process [6] of figure 1.

Stage (i) and (ii) conditions are much the same here, with all components active, but during stage (iii), as vortices move away from the bar, the first term on the right-hand side disappears. When using infinite-domain mutual advection relations (2.1), vortex transport during stage (iii) conditions is always towards the centre of the gap. *Thus, for shore-normal waves, longshore vortex transport, like cross-shore transport, appears completely dependent on the detailed geometry of the bar–trough–gap system, and waves are only important in that, by breaking with a given strength in a given location, they generate circulation.*

Equation (2.11) was derived using (2.1) as the basis for the mutual advection between vortex [1] and [4]. Using this approximation, vortices [2–3] induce no longshore velocity in vortex [1] because of their purely circular orbits. However, examination of figure 2 shows that the full relations have orbits with a significant longshore component at the same cross-shore location as the vortex core. Thus, vortices [2–3] may induce a significant longshore motion on vortex [1], particularly when the gap or crest lengths, L_c, L_t, are small. Both vortex [2] and [3] tend to move vortex [1] towards the crest. Vortex [4] continues to move vortex [1] towards the gap.

Schematically, the longshore velocity of vortex [1] using the full relations becomes

$$V_1 = V_{sa6} + V_{sa7} + V_{ma2} + V_{ma3} + V_{ma4} \tag{2.12}$$

where V_{ma2-4} are computed using (2.2)–(2.3). During stage (iii) conditions, V_{sa6} disappears. Of course it is possible to include others of the infinite number of vortices that have some effects on vortex [1] in a periodic bar–gap system, but we have included only the major components. The greatest remaining source of error here is likely to be the effect of three-dimensional topography which is very difficult to quantify simply.

2.3.1. *Relative importance of self-advection* [7] *and mutual advection* [4]

When the distance of vortex [4] from the shoreline is much smaller than the crest distance, $x_{sv} \ll x_b$, then the mutual advection term V_{ma4} is greatly changed from the infinite-domain results. Again using asymptotic relations for small m, vortex [4] induces a longshore motion of vortex [1] toward the gap which can be obtained by means of (2.6):

$$V_{ma4} = \left[\frac{1}{d}\frac{\partial \psi}{\partial x}\right]_{x=x_b} = \frac{\Gamma x_{sv}^2}{4x_b^3}, \tag{2.13}$$

which is about $(x_{sv}/x_b)^2$ times smaller than the infinite-domain value of (2.10).

Now, during stage (iii) conditions, the longshore velocity of vortex [1] is composed only of mutual advection from vortices [2–4] and self-advection from the sloping bed, and has a value of

$$V_1 = -\frac{\Gamma}{4x_b}\left\{\underbrace{\left(\frac{x_{sv}}{x_b}\right)^2}_{V_{ma4}} + \underbrace{\frac{1}{\pi}\left[\log\left(\frac{8x_b}{R}\right) - \frac{1}{4}\right]}_{V_{sa7}}\right\} + V_{ma2} + V_{ma3}. \tag{2.14}$$

The quantity in the square brackets varies in a relatively small range – from 2.25 to 4 – for plausible values of x_b/R from 1.5 to 9. We thus make the approximation that the value of the bracketed quantity is π, to arrive at

$$V_1 = -\frac{\Gamma}{4x_b}\left[1 + \left(\frac{x_{sv}}{x_b}\right)^2\right] + V_{ma2} + V_{ma3}. \tag{2.15}$$

This is extremely crude but, since the scaling assumes $O(x_{sv}/x_b) = O(\epsilon) \ll 1$, it then becomes clear that self-advection along the sloping bed dominates over mutual advection from vortex [4] when vortex [4] is close to the shoreline.

2.3.2. *Longshore transport of shore vortex* [4]

While both mutual advection and self-advection during stage (iii) conditions tend to move vortex [1] away from the bar and towards the centre of the gap, shore vortex

[4] has two opposing processes acting upon it: self advection with the shoreline [7] acting towards the centre of the bar, and mutual advection with vortex [1] acting towards the centre of the gap.

If the distance of vortex [4] from the shoreline, x_{sv}, is comparable to the bar crest distance, x_b, then the shore-vortex longshore velocity is given by the infinite-domain relations

$$V_4 = \frac{\Gamma}{4\pi}\left\{\frac{2}{(x_b - x_{sv})} - \frac{1}{x_{sv}}\left[\log\left(\frac{8x_{sv}}{R_{sv}}\right) - \frac{1}{4}\right]\right\}. \tag{2.16}$$

Once again taking the quantity in the square brackets to vary between 2.25 and 4, there is a zero point in longshore transport during stage (iii) conditions at somewhere in the range

$$\frac{9}{17} \leqslant \frac{x_{sv}}{x_b} \leqslant \frac{2}{3}. \tag{2.17}$$

If the shore vortex is not near the bar crest and instead $x_{sv}/x_b \ll 1$, asymptotic approximations to (2.6) give

$$V_4 = V_{ma1} + V_{sa7} = \frac{\Gamma}{2x_b} - \frac{\Gamma}{4\pi}\frac{1}{x_{sv}}\left[\log\left(\frac{8x_{sv}}{R_{sv}}\right) - \frac{1}{4}\right]. \tag{2.18}$$

Again taking the quantity in the square brackets in (2.18) to be between 2.25 and 4, we find that for zero longshore velocity of vortex [4] it is $9/8\pi \leqslant x_{sv}/x_b \leqslant 2/\pi$, which is similar to the infinite-domain mutual advection case.

For both cases, when vortex [4] is closer to the shoreline it tends to travel towards the centre of the bar, and when it is closer to the bar crest, it tries to travel towards the gap. Because the longshore velocity of vortex [4] comes from the difference of two similarly valued quantities, it is predicted to be relatively small when the vortex is approximately midway between the bar and shoreline.

From (2.7), replacing the bar crest position x_b by the shore-vortex position x_{sv}, cross-shore transport of vortex [4] is predicted to be relatively small, except when $O(x_{sv}) = O(L_t, L_c)$. Because vortex [4] is closer to the shoreline than the bar crest, this only occurs for extremely narrow gaps or crest lengths.

2.3.3. *Applicability of relationships*

The many relations for cross-shore and longshore transport given in the preceding sections all contain significant approximations and, thus, it is helpful to explore at least qualitatively their uses and limits. During stage (iii) conditions, the most obvious limitation is that the effects of three-dimensional topography are ignored. This was justified by assuming that bar effects disappear as soon as vortex [1] leaves the bar crest and enters the gap. In reality, there are lingering effects that are presumably much smaller than when vortex [1] is near the three-dimensional bar, but this remains a source of error.

A more general source of complication concerns consecutively generated vortices. As was seen in figures 3 and 4 of Part 1 and also shown in figures 7–13 in the following ([99] indicating the location of consecutively generated vortices), multiple vortices are generated from the same location after a relatively short time. In some case (e.g. case (2) of figure 10) we may treat these as one big vortex with one or two cores, but again this introduces errors making application of theoretical relationships more difficult.

A further source of uncertainty is introduced by the change in geometry of vortices as they travel away from their generation points. For example, as vortex [1] travels

toward the centre of the gap its oppositely signed counterpart, vortex [2], travels to meet it. As the distance between the two becomes smaller, their cross-shore mutual advection increases and, at some point, the vortex couple always begins to travel offshore. Thus, the velocity relationships derived earlier change with time. This point is to be explored further in § 3, when these simplified predictive methods are compared with observed vortex tracks in the laboratory and computed tracks using a Boussinesq wave model.

Overall, the general relationships predicted from our analyses, i.e. directions of travel and relative strengths of longshore and cross-shore velocities, will be shown in § 3 to be remarkably robust: these predictions of vortex transport can be a good descriptor of the overall processes beyond the conditions for which they were derived. This is significant and means that the relatively simple analyses may give a good prediction of the overall vorticity transport.

Relations such as those developed here may also be used to examine the overall character of the flow. By evaluating velocities at locations other than the vortex core, features such as feeder currents and offshore-directed flow in the gap are certain to appear. As a qualitative example, in the centre of the gap between vortices [1] and [2], longshore flow is zero (from symmetry), while examination of the sense of the vortices in figure 1 and the streamlines of figure 2 shows strongly offshore flow arising from vortices [1–2], while shore vortices oppose this slightly to moderate the strength of the offshore-directed current. This offshore-directed current in the gap has been previously shown in many more complex numerical computations (e.g. Haas *et al.* 2003) and laboratory experiments (e.g. Haller & Dalrymple 2001).

3. Laboratory and numerical experiments

Laboratory and numerical experiments were used to test predictions from § 2. Laboratory experiments used video-tracked floating drifters with the general setup of Kennedy & Thomas (2004), but with topographies ranging from narrow rip currents to an isolated bar. Numerical experiments with time-domain Boussinesq-type equations were used to gain additional information on vortex trajectories.

The topographies tested

Figure 3 shows the three topographies tested. Case (1) is a narrow rip current topography, and is the same geometry as found in Haller & Dalrymple (2001) and Kennedy & Thomas (2004): a 1:30 slope superimposed with a two-rip-channel bar system with nominal bar crest depth of 4.73 cm, and maximum bar height of 0.06 m. Case (2) widens the gap width L_t and thus narrows the crest length L_c. Case (3) removes completely the side bars, giving an isolated bar. Because bar cross-sections are identical, with only lengths and gap widths varying, the influence of geometry on vortex paths becomes clear. Table 1 gives a summary of important geometrical properties for each case. Although case (3) has only one bar, an effective gap width is found here by considering the vertical sides of the basin as an axis of symmetry.

A short description of the laboratory experiments

One forcing was used for all cases. This is given by the single wave group shown in figure 4 which represents the free-surface position at $(x, y) = (6.0, 16.2)$ m, i.e. around 5 m offshore of the bars. The nominal group length at the wavemaker was 64 waves with period $T = 1$ s including a 10 wave linear ramp-up and abrupt cessation. Based on measured heights, the equivalent deep water wave steepness was $(H/L)_0 = 0.035$, and wavelengths at the bar crest were approximately 0.66 m.

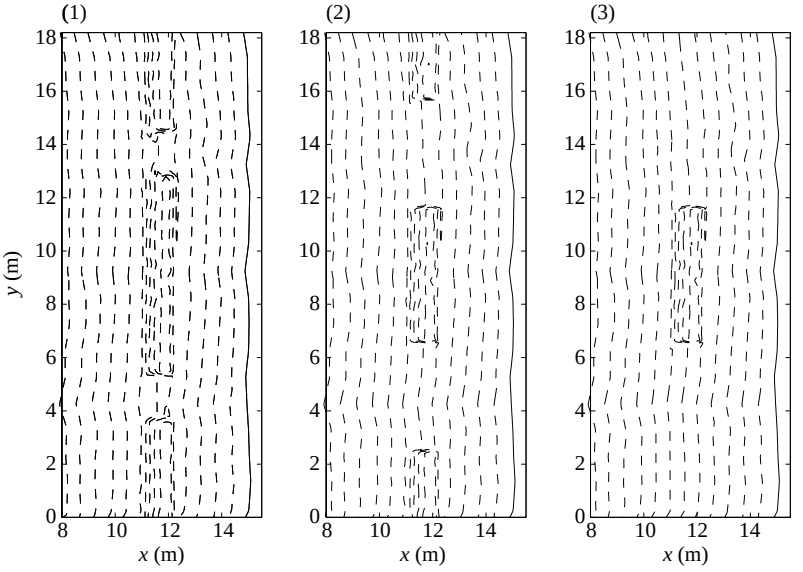

FIGURE 3. Bathymetry contours (2 cm) for cases (1)–(3). Shoreline is the solid line at the right of each plot.

Setup	L_t (m)	L_c (m)	x_b (m)	x_{sv} (m)
(1)	1.80	7.31	2.9	1.4
(2)	4.24	4.87	2.9	1.4
(3)	13.35	4.87	2.9	1.4

TABLE 1. Geometrical properties for laboratory tests.

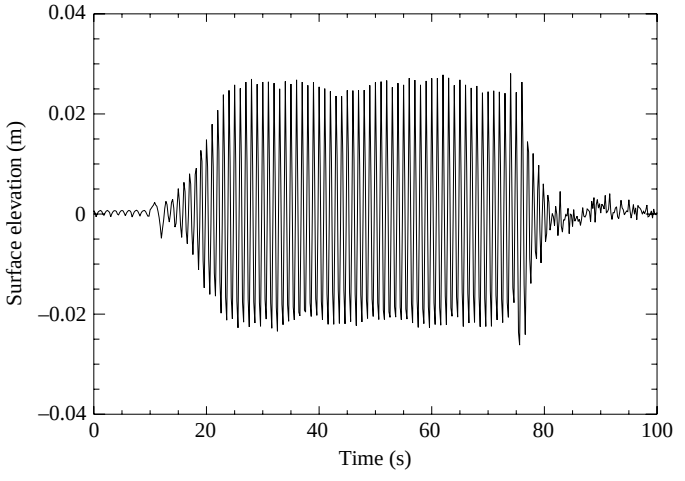

FIGURE 4. Time series of wave forcing for all cases at $(x, y) = (6.0, 16.2)$ m.

Drifters used were the same as in Kennedy & Thomas (2004): swimming pool lane dividers with diameter $D = 10.7$ cm and thickness $w = 1.7$ cm. For the wave conditions used, drifters of this size were small enough that they did not interfere significantly

Case	$(U_1,V_1)/\Gamma(1/\mathrm{m})$					
	u_{inf}	v_{inf}	u_{full}	v_{full}	$(u/v)_{inf}$	$(u/v)_{full}$
(1)	−0.067	0.19	−0.064	0.067	−0.35	−0.96
(2)	−0.025	0.19	−0.004	0.084	−0.025	−0.048
(3)	0.021	0.19	0.01	0.099	0.11	0.10

TABLE 2. Predicted initial ratios of cross-shore and longshore velocities for vortex [1] during stage (iii) conditions. Subscript *inf* denotes computations using infinite-domain relations ((2.1), (2.11)), while *full* computations use ((2.7), (2.14)).

with the large-scale flow, but large enough and with weak enough flotation that they did not surf directly to shore in breaking waves. Drifters were tracked at 3 Hz and low-pass filtered at 0.33 Hz to remove the effect of wave orbital velocities. Tracks in the image coordinates were rectified to the Cartesian still-water level using a direct linear transformation (DLT) (e.g. Holland *et al.* 1997). Drifter tracks are suitable both for qualitative evaluation of flow patterns and quantitative analysis. Overall, this setup has been found to approximate well the surface mass transport velocities by low-pass drifter velocities (Kennedy & Thomas 2004).

A short description of the numerical experiments

Because of concerns about their ability to reproduce accurately breaking locations on complex geometries and thus generate realistic shore vortices, the shock-capturing, phase-resolving nonlinear shallow water equations (NSWE) of Part 1 (see also Brocchini *et al.* 2001) were not employed here. Instead, a time-domain Boussinesq-type model was used, which reproduces breaking locations more accurately. Computations used the datum-invariant extended equations of Kennedy *et al.* (2001) combined with the surf zone extensions of Kennedy *et al.* (2000) and Chen *et al.* (2000). Together, these reproduce correctly leading-order vorticity generation and transport from wave breaking as discussed in Part 1. A slightly different form of these governing equations has been shown to work well on the same geometry as in case (1) by Chen *et al.* (1999), but with different wave forcing.

There was one notable difference from the physical experiments: the sidewalls at $y = (0, 18.2)$ m were removed, the domain width was doubled using symmetry about the removed walls, and the bathymetry was then made periodic in the longshore. These sidewalls are necessary for a physical model, but eliminate the possibility of antisymmetric instabilities about the sidewalls and for this reason were removed in the computations. A model grid size of $(\Delta x, \Delta y) = (0.05, 0.05)$ m and time step $\Delta t = 0.01$ s were used in all tests.

3.1. *Directions of vortex transport*

The relations of § 2 may be used to predict magnitudes and directions of travel for vortex [1] as geometries change. We are most interested in stage (iii) conditions when mutual advection and self-advection with the shoreline dominate, as this stage represents the beginning of large-scale vorticity transport. The predicted direction of longshore transport is always towards the gap, but as the gap width L_t increases and the retarding effect from vortex [2] decreases, the predicted longshore velocity of vortex [1] increases significantly. As the gap width L_t widens and crest length L_c narrows, the predicted direction of cross-shore transport varies from offshore to onshore. Table 2 and figure 5 give predictions of stage (iii) vortex transport in relation

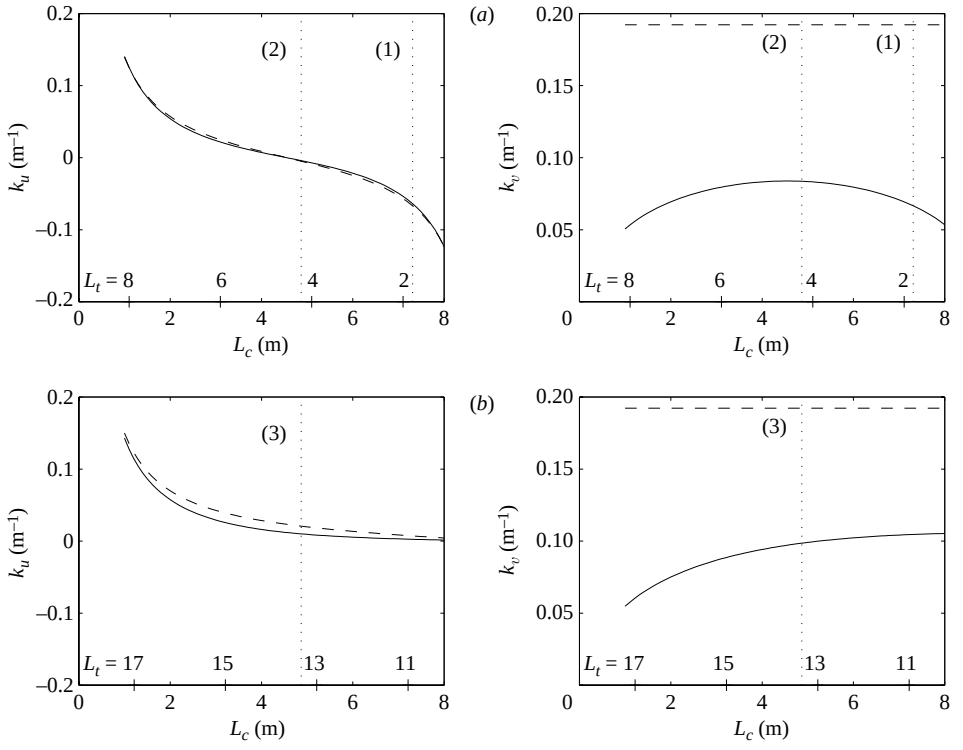

FIGURE 5. Predicted initial cross-shore and longshore velocities during stage (iii) conditions, where $(U_1, V_1) = \Gamma(k_u, k_v)$. —, full relations; ——, infinite-domain relations. (*a*) Two bars in the laboratory system; (*b*) one bar in the laboratory system. Vertical dotted lines indicate the cases tested.

to the circulation of vortex [1] using both infinite-domain relations ((2.1), (2.11)) and sloping-bed relations ((2.7), (2.14)).

Thus, while the longshore vortex transport is predicted to always be strongly towards the gap, initial cross-shore transport is predicted to change continuously from strongly offshore with the narrow rip current topography of case (1) to weakly onshore with the isolated bar of case (3). Predicted longshore transport increases as the gap width increases and crest length decreases. Thus, the system is predicted to vary smoothly from the strong offshore and weak longshore transport of case (1) to strong longshore and weak cross-shore transport in case (3).

We may make more specific observations: for the two-bar cases (cases (1)–(2)) cross-shore transport appears to be predicted well by the infinite-domain relations, but this is not true for the one-bar setup (case (3)). This is because in the two-bar setup there is almost always one dimension, either the crest or gap length, that is small. Here, the interaction is strong and the infinite-domain relations are applicable; thus the good agreement between both estimates. For the one-bar setup, agreement is good when the bar crest length, L_c, is small but becomes worse as the crest length increases. Still, the overall predicted cross-shore transport here is small so, although the differences are large in relative terms, the absolute error remains small.

For longshore transport of vortex [1], there are great differences. Infinite-domain relations show strong transport from shore vortex [4], and are also without the retarding effects of vortices [2–3]. Thus, transport here is predicted to be strong

and invariant with respect to crest and gap dimensions. Full relations show much weaker longshore transport that is strongest when crest and trough lengths are equal. Longshore transport is also stronger for the single-bar case as the extremely long gap lengths, L_t, mean that the retarding influence of vortex [2] is small.

Figure 5 can also give a rough indication of the effective changes in geometry as vortices travel away from the areas where they were generated. For all geometries, vortex [1] travels towards the gap centre, which decreases the effective gap width, L_t, over time. This, in turn, increases the tendency towards offshore transport. This change in effective geometry is particularly apparent for case (2) where initial predicted cross-shore transport is quite small, but longshore transport is strong and thus offshore transport increases quickly over time. Here, strong changes are seen in the vortex paths over relatively short periods.

A more complete description of changing effective geometries may be found by using predicted longshore and cross-shore velocities to integrate vortex trajectories through time, i.e. $\mathrm{D}\boldsymbol{X}/\mathrm{D}t \equiv (U, V)$. Since velocities change with changing vortex positions, curves followed by the vortices may be predicted numerically. This analysis has the further advantage that if the relative circulations of vortices [1], [2], etc., remain the same, the paths taken are invariant with the overall strength of the system.

For these reasons, and as a severe test of the transport relations, trajectories of vortex [1] (and thus from symmetry [2–3]) were computed for the three test cases. Explicitly, $U_1 = U_{ma2} + U_{ma3}$, $V_1 = V_{sa7} + V_{ma2} + V_{ma3} + V_{ma4}$. For the self-advection term, V_{sa7}, the term in the square brackets of (2.9) was approximated as π, so that $V_{sa7} = -\Gamma/(4x_b)$. To demonstrate the overwhelming importance of geometry on transport paths, one further approximation was made: the shore vortex [4], which was predicted to have small velocity, was fixed at its original location. Starting locations were taken as the shoreward edge of the bar, where stage (iii) conditions are likely to begin.

These approximations are sweeping and rather drastic. In addition to the geometrical simplifications, they neglect processes which are known to be significant such as frictional dissipation and successively generated vortices. However, despite all of this, comparisons with measured and computed tracks will show that the simplified predictions are surprisingly robust. Note that, as also shown by Bühler & Jacobson (2001), frictional contributions are small with respect to advective accelerations during the early stages of motion. In fact the dissipative scale d/f (f being a Chezy-type frictional coefficient of order 0.01) is about one order of magnitude larger than the advective scale R. Still, dissipation is clearly visible in later time stages of the simulations to follow.

Figures 6, 9 and 12 show measured sequences of drifter tracks for cases (1), (2) and (3) respectively. Corresponding numerical results are reported in figures 7, 10 and 13. These are discussed in detail with the aim of illustrating and quantifying the flow transition which occurs when increasing the gap size from that of the narrow rip-current case (1) to that of the isolated breakwater (3).

3.1.1. *The narrow rip-current case* (1)

The narrow rip-current topography of figure 6 shows clearly the development of the bar vortices [1–2], shore vortex [4] and its counterpart; vortex [1] can be seen clearly in the tracks of the looped drifter on the lower side of the gap in figure 6(a, b). Note that because of camera limitations, only around half of the laboratory domain is shown. A slight movement towards the gap centre is visible, but by far the strongest

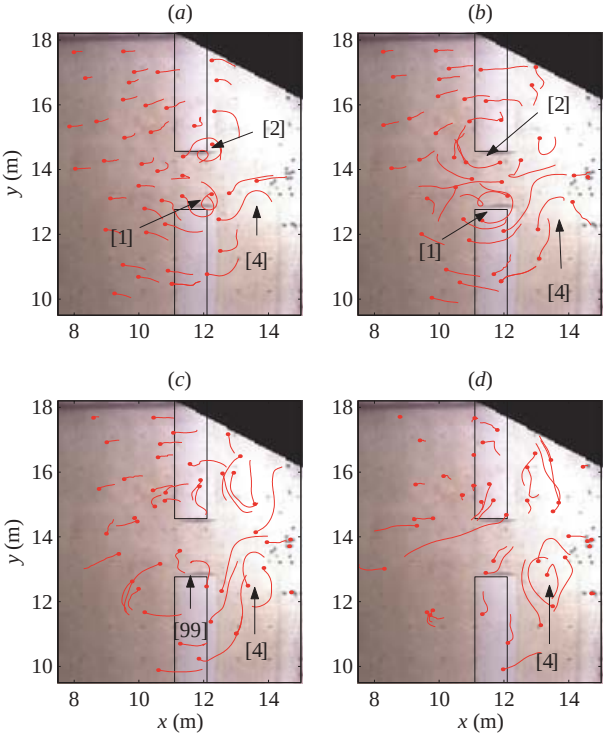

FIGURE 6. Startup pathlines for selected drifters in case (1). (*a*) 0–30 s, (*b*) 30–60 s, (*c*) 60–90 s, (*d*) 90–120 s. Solid circles give the beginning point of each pathline. Arrows denote identifiable vortices [1], [2], and [4]. Vortex [99] shows signs of a consecutively generated vortex.

vortex motion is offshore, as was predicted in table 2 and figure 5. Shore vortex [4] appears to stay mostly in place even after forcing stops, adding weight to predictions that shore vortices have relatively weak migration speeds. Overall, the flow follows very well predicted modes of behaviour in table 2 and figure 5.

Results of the numerical computations give a very similar picture, both qualitatively and quantitatively, but with much more detail. Figure 7 gives the instantaneous streamlines and vorticity snapshots through the various stages of the flow. One general feature of the numerical data is the generation and evolution of vortical structures of various sizes and intensities in addition to the large vortices [1–4]. In part, this is because of small-scale irregularities in the laboratory bathymetry which, in turn, leads to small variations in breaking intensity – a visible feature in the laboratory. Even with these irregularities, the generation of bar and shore vortices [1–2,4] is very clear.

Figure 7(*a*) shows the startup conditions (stage (i)) for the flow. In particular we focus on the uppermost pair (see arrows), vortices [1–2], as these are the pair imaged on video. By the end of part (*a*), these are formed and distinct on the bar ends. Initial transport again has significant offshore and longshore components, but becomes more offshore in frames (*b–d*). By part (*b*), the shore vortex [4] is evident and influencing the motion of [1]. The beginnings of consecutively-generated vortices are also clearly visible in (*b*) and may be tracked through frames (*c*, *d*).

Figure 8(*a*) shows a direct comparison between computed Boussinesq, laboratory, and predicted vortex tracks using the simplified methods. Tracks are broadly similar,

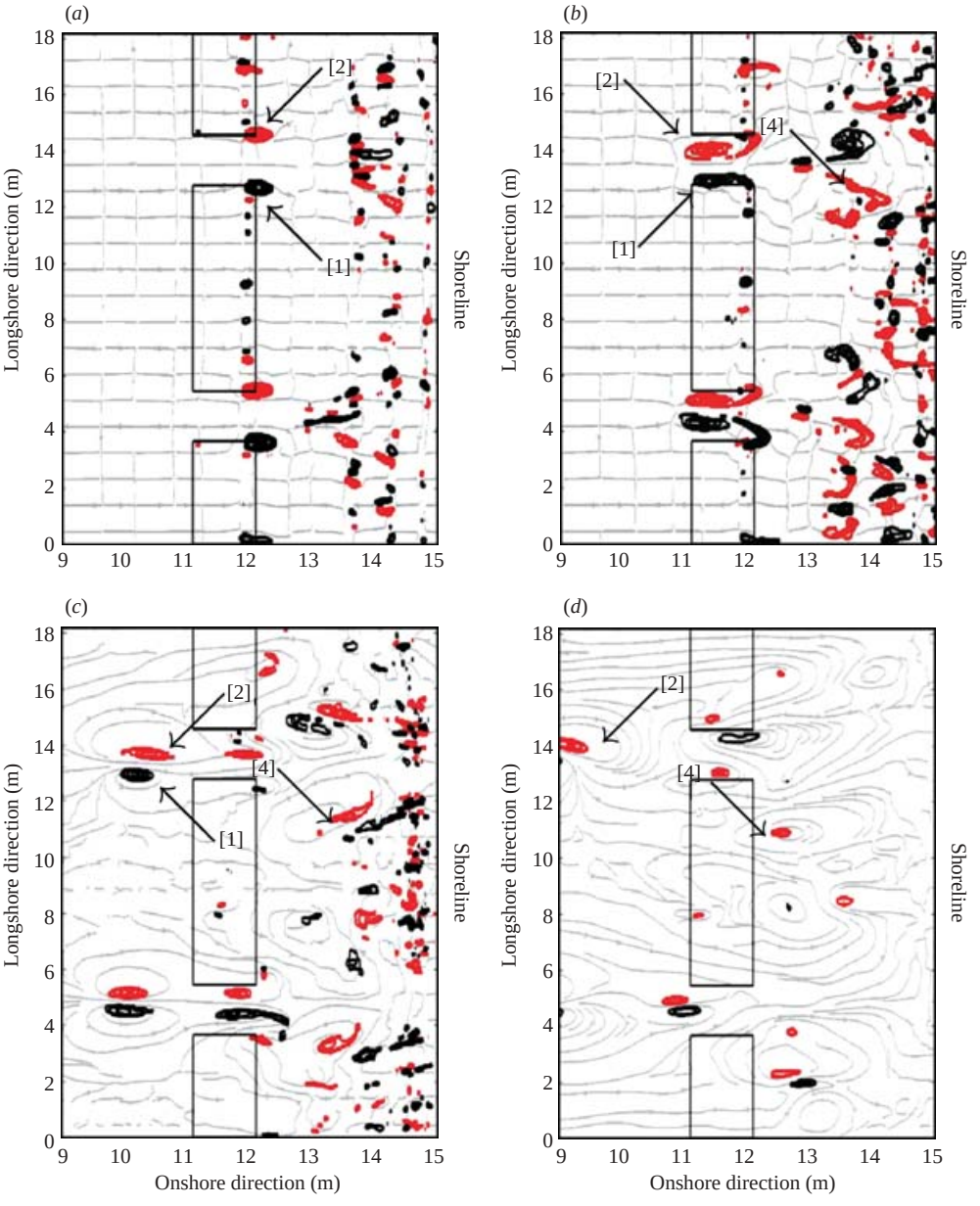

FIGURE 7. Flow patterns and shoreward macrovortices migrations for flow conditions of case (1). From left to right and from top to bottom the contour plots of the vorticity field are superposed onto the instantaneous streamlines for times $t = 30, 60, 80, 105$ s. Vorticity contour lines are black for positive (counterclockwise) vorticity and red for negative (clockwise) vorticity with contour interval of $0.5\,\mathrm{s}^{-1}$. Coordinates are distorted.

with vortices moving from the shoreward bar corners towards the gap centre and offshore, and longshore motion decreasing with increasing offshore distance. However, longshore asymmetries in the Boussinesq and laboratory tracks are not reproduced in the simplified predicted results, which are symmetric about the gap. These asymmetries are almost certainly because of small three-dimensionalities in the underlying concrete

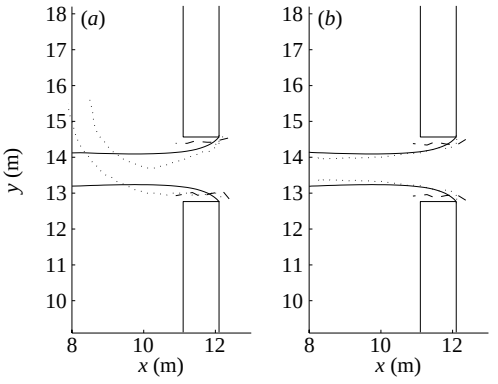

FIGURE 8. Computed Boussinesq (...), measured drifter (——), and predicted simplified (—) vortex tracks for test case (1). (*a*) Raw data; (*b*) symmetric components of tracks.

Case	Simplified	Laboratory	Boussinesq
(1)	±21.0	−4.5, 6.3	−12.8, 32.5
$(1)_s$	±21.0	±5.3	±23.3
(2)	±51.6	−37.5,39.0	−43.7, 60.9
$(2)_s$	±51.6	±38.8	±54.6
(3)	−91.4	−84.6	−89.0

TABLE 3. Angles of integrated vortex paths for cases (1)–(3), $\theta \equiv \tan^{-1}((y_2 - y_1)/(x_2 - x_1))$. Negative angles are results for vortex [1], while positive angles are for vortex [2]. Subscript *s* denotes the symmetric components of the vortex travel.

floor of the basin (Haas & Svendsen 2002), which are not included in the simplified predictions. Their neglect appears to be the major source of error in the simplified predictions, particularly as offshore distances increase, and their major effect appears to be to introduce an antisymmetric component into the vortex tracks.

Because asymmetries are relatively mild while the vortices are close to the bar, the Boussinesq and laboratory tracks may be separated into symmetric and antisymmetric components (see Appendix B). Figure 8(*b*) shows both raw and symmetric vortex tracks. Although there are minor differences, all three tracks appear quite similar. An overall measure of accuracy may be found by comparing the cumulative angles of the vortex tracks, i.e. $\tan^{-1}((y_2-y_1)/(x_2-x_1))$, where y_2 is the longshore location of the vortex at the end of integration. Because laboratory tracks ended just offshore of the bars, $x_2 = 11$ m was taken as the offshore limit for the integration, and (x_1, y_1) is the vortex location at the presumed start of stage (iii) conditions (at the shoreward bar corner for all cases here). Table 3 gives integrated angles for both the raw and symmetric results, while figure 8(*b*) shows symmetric results graphically. Symmetric Boussinesq angles are within 3° of the simplified solutions, while laboratory results show vortices travelling more directly offshore, with a difference in direction of over 15°. This reduced relative longshore/increased cross-shore motion in laboratory tests is also seen in the other two cases, even though all three methods predict identical trends with increasing gap length.

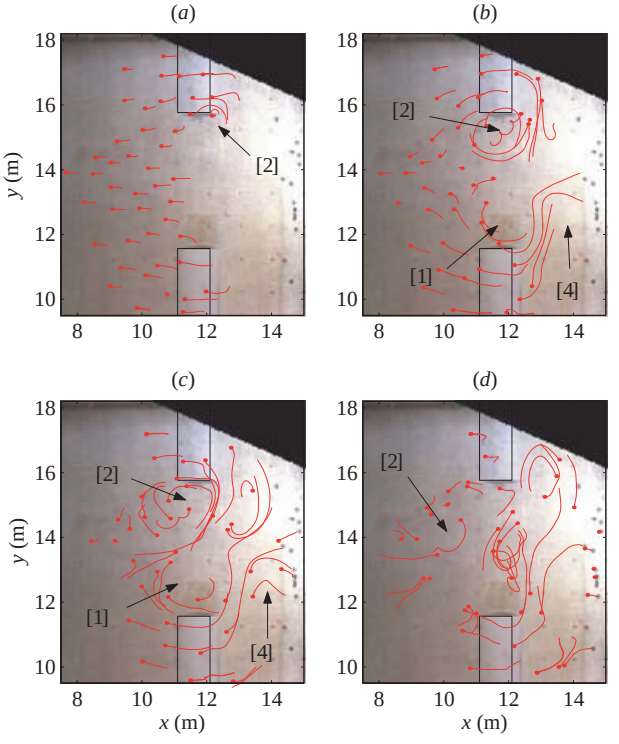

FIGURE 9. Startup pathlines for selected drifters in case (2). Labels and time intervals are the same as in figure 6.

3.1.2. *The wider rip-current case* (2)

When compared to case (1), case (2) has a wider gap, L_t, and correspondingly shorter crest length, L_c. This means that initial cross-shore transport is predicted to be small, but still weakly offshore. Both of figures 9 and 10 show initial cross-shore transport to be significantly weaker than in figure 6, and with a stronger longshore component, confirm predictions. Overall, the figures show a flow that still resembles a rip current, but one that is elongated. A strong initial longshore transport then becomes much stronger offshore as vortices [1–2] approach each other, demonstrating the changing effective geometries. This, because of mutual advection, tends to increase offshore transport and decrease longshore transport, as demonstrated in figure 5. Overall, the trend of change from case (1) is predicted well, as longshore transport does become stronger and cross-shore transport weaker.

The numerical results of figure 10 confirm the laboratory results. Initial transport is clearly more towards the centre of the gap than in case (1), which adds further confirmation to the trends predicted by the simplified model. Cross-Shore transport then increases strongly with a slight asymmetry as was also observed in the laboratory.

Comparisons between the three methods are given in figure 11, which shows raw and symmetric components of vortex tracks. Once again raw Boussinesq and laboratory tracks in (*a*) follow the trends of the simplified predictions, with initial longshore transport considerably stronger than in case (1). However, a longshore asymmetry is again visible in the Boussinesq and laboratory tracks but not in the simplified predictions. After its removal in (*b*), all three tracks show an improved match although once again differences do remain. Table 3 provides quantitative data

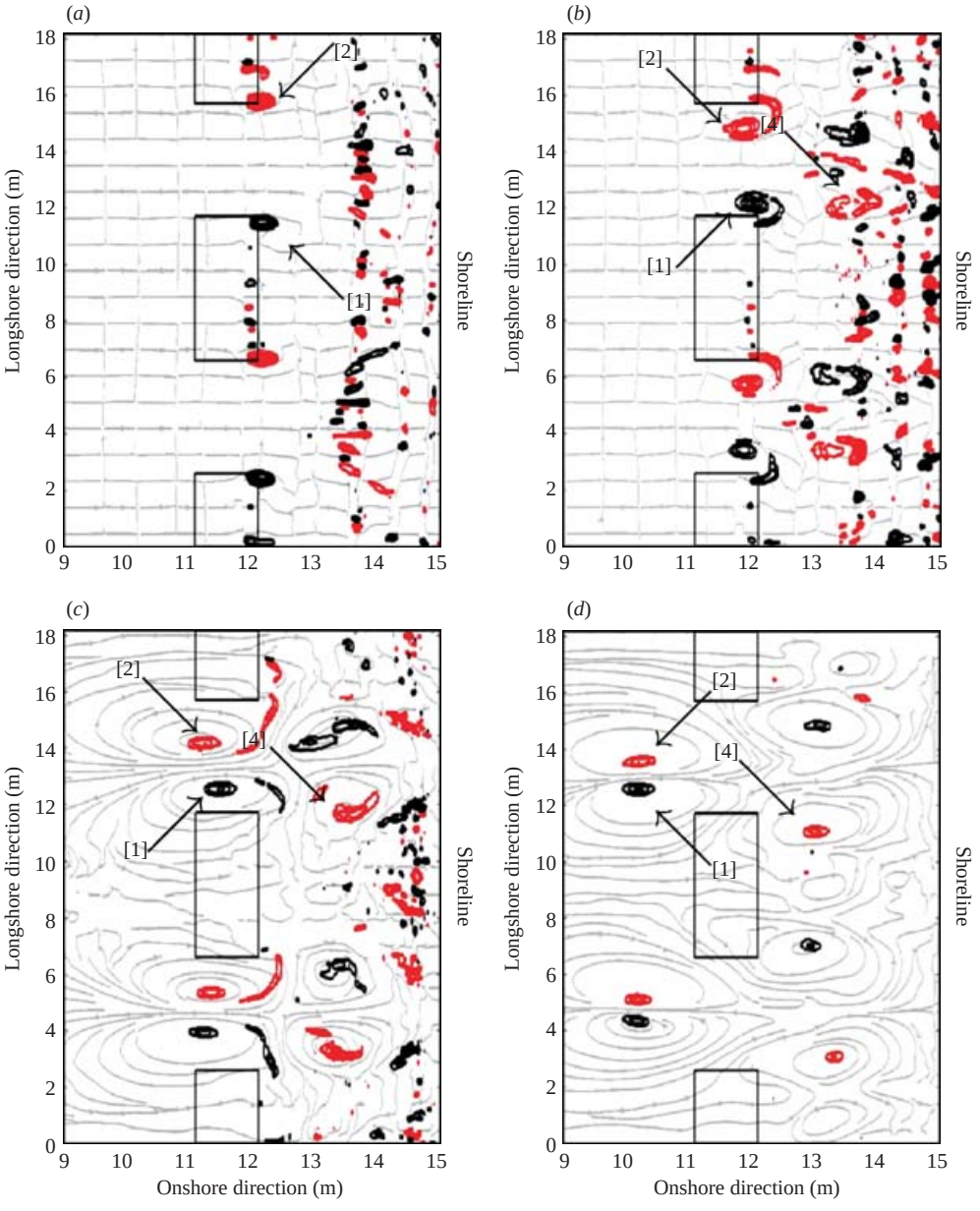

FIGURE 10. Flow patterns and shoreward macrovortices migrations for flow conditions of case (2). From left to right and from top to bottom the contour plots of the vorticity field are superposed onto the instantaneous streamlines for times $t = 30, 60, 80, 105$ s. Vorticity contour lines are black for positive (counterclockwise) vorticity and red for negative (clockwise) vorticity with contour interval of $0.5\,\mathrm{s}^{-1}$.

on the integrated angles. All measurements and predictions show stronger longshore transport demonstrated by the increased angles compared to case (1). After removing the antisymmetric component, Boussinesq angles are within 3° of the simplified predictions, while laboratory tracks again show directions more than 10° further offshore. The difference between simplified predictions and laboratory data might

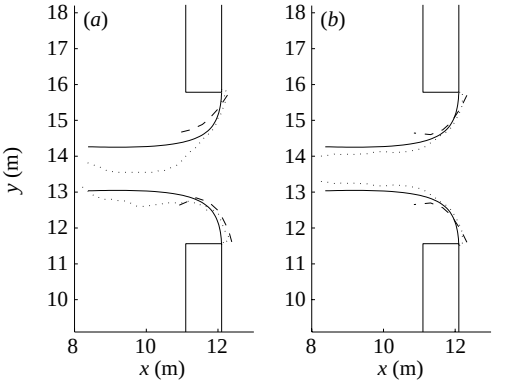

FIGURE 11. Vortex tracks for test case (2) for (*a*) raw data; and (*b*) symmetric components. Line styles are identical to figure 8.

be expected, as the simplified method neglects many processes, but the discrepancy between Boussinesq and laboratory results is less expected because of the general nature of the model. The most important process not included in the Boussinesq model is the effect of depth-varying currents. For the narrow rip-current geometry, this is known to be significant (Haas *et al.* 2003), and we hypothesize that it is the leading source of these differences. However, no definitive conclusions may be reached with the available data.

3.1.3. *The isolated breakwater case* (3)

Figure 12, which gives laboratory results for the effectively isolated breakwater in case (3), is very different from cases (1) and (2), which both resembled to some degree rip currents. Cross-Shore transport of vortex [1] is virtually non-existent through parts (a–c), when compared with longshore transport. A small offshore motion can be seen in panel (*d*), when vortex [1] approaches the wall at $y = 18.2$ m, and its image produces a vortex couple which starts to advect it offshore. (Results from times later than this have increasingly strong rip-current development as vortex [1] approaches the wall.) As predicted, shore vortex [4] has little net transport, perhaps with a small motion towards the bar ends. The numerical results of figure 13 confirm this, with almost total longshore motion of vortex [1] throughout the simulation. Together, cases (1)–(3) demonstrate the overwhelming effects of bar and gap length geometry on vortex paths, where geometries with identical wave forcing and bar cross-sections show entirely different behaviours.

Track predictions from the simplified method shown in figure 14 once again agree with the Boussinesq and measured results: an almost total longshore transport that very slowly turns offshore as the vortex approaches the wall. As with cases (1) and (2), measured tracks show a slightly greater offshore motion than the simplified predictions and the Boussinesq computations. However, overall agreement is the best of the three cases. Integrated angles (from vortex start to $y_2 = 14.5$ m) given in table 3 for all three methods give angles within 5° of each other. This provides additional confidence in the simplfied method's ability to predict well overall behaviours.

4. Conclusions

Computations and experiments have demonstrated a wide range of behaviours for breaking-wave-generated, topographically controlled macrovortices. Longshore vortex

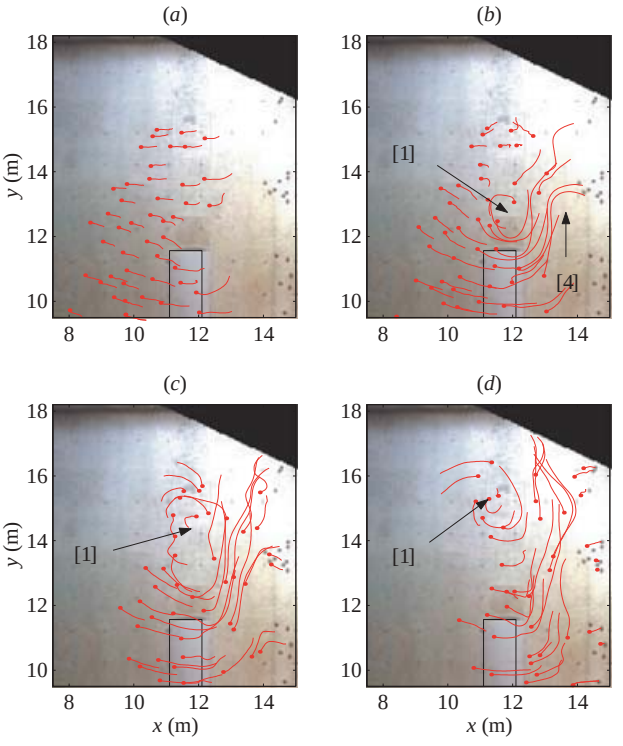

FIGURE 12. Startup pathlines for selected drifters in case (3). Labels and time intervals are the same as in figure 6.

transport was found to be controlled in large part by mutual advection between oppositely signed vortices on the bar ends, and by self-advection with the sloping shoreline. Mutual advection with shore vortices was predicted to play a secondary role. Overall, as the system transitions from a narrow rip-current topography to an isolated breakwater, initial directions of macrovortex transport also change from strongly offshore to strongly longshore.

This transition was found to be predicted well by relatively simple relations that modelled transport as arising from a small number of vortices generated at bar ends and near the shoreline. Expressions that only considered mutual interactions between vortices and self-interaction with the sloping shoreline gave surprisingly good agreement with laboratory measurements and computations using a Boussinesq wave model. Considering all three cases together, these simplified methods have fair accuracy in predicting detailed vortex paths, as neglected processes sometimes meant that details of simplified predictions sometimes showed error; with differences in integrated angles of vortex travel up to 15°, we may have reached the limit of what simple expressions may accomplish. Chief among the neglected processes are likely to be consecutively generated vortices, three-dimensional topographic effects and topographic irregularities, depth-varying currents, and bottom friction.

However, the simplified methods predicted extremely well the changes in behaviour as gap lengths increased and crest lengths decreased. In all situations considered, the overall character of the flow was predicted well, whether a strongly offshore rip current or a strong longshore current. We believe that this demonstrates conclusively the overwhelming importance of geometrical factors on the flow, and also that relatively

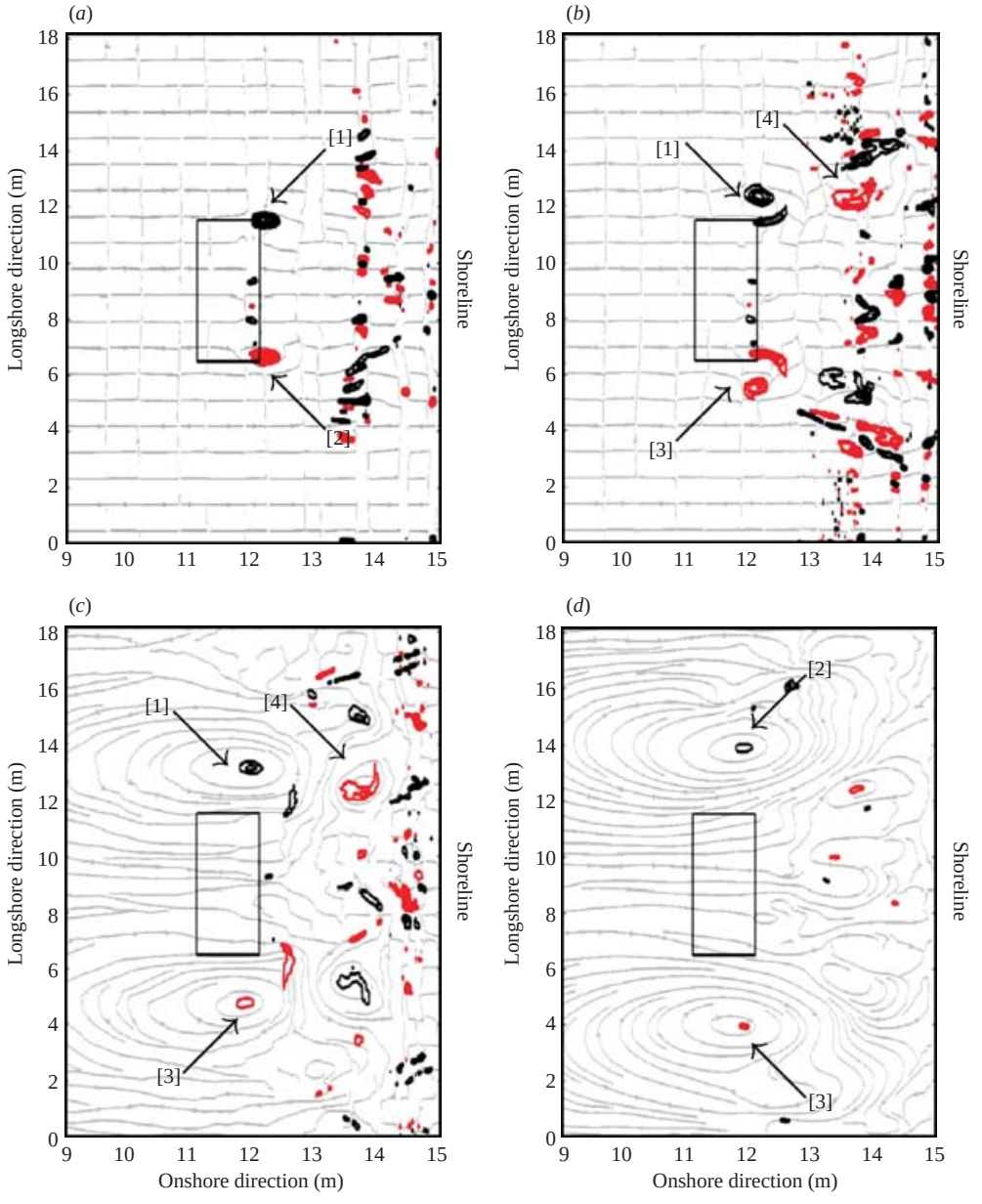

FIGURE 13. Flow patterns and shoreward macrovortices migrations for flow conditions of case (3). From left to right and from top to bottom the contour plots of the vorticity field are superposed onto the instantaneous streamlines for times $t = 30, 60, 80, 105$ s. Vorticity contour lines are black for positive (counterclockwise) vorticity and red for negative (clockwise) vorticity with contour interval of $0.5\,\mathrm{s}^{-1}$.

few simple processes may also predict with good accuracy the overall character of vortex travel.

Very large differences were found in predicted longshore transport rates between infinite-domain vortex representations (as were used in Part 1) and more complete

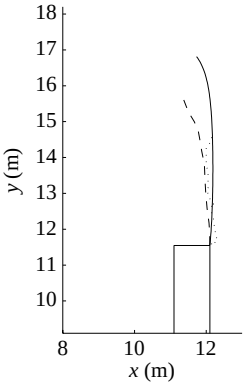

FIGURE 14. Computed Boussinesq (- - -), measured drifter (···), and predicted simplified (—) vortex tracks for test case (3).

representations taking into account the sloping bed. In contrast, predicted cross-shore transport rates were surprisingly similar for both representations.

Work by A. B. K. and E. G. was supported by the University of Florida. A. B. K. received further support from the National Oceanographic Partnership Program under grant N00014-99-1-1051. M. B. was supported by the European Commission Research Grant EVK3-2000-22038 (DELOS) and by the Italian MIUR Grant "Influenza di vorticità e turbolenza nelle interazioni dei corpi idrici con gli elementi al contorno e ripercussioni sulle progettazioni idrauliche". L. S. was supported by the Italian MIUR Grant "Idrodinamica e morfodinamica di spiagge protette da opere tracimabili". The University of Delaware's donation of facility time is also gratefully acknowledged.

Appendix A. Strength of shore vortices

The relative strengths of bar vortex [1] and shore vortex [4] depend on details of wave breaking. If diffraction, refraction, and wave–current interaction are not significant, then the strength of vortex [1] is given by the appropriate version of (2.19), (2.21), or (2.23) of Part 1. The height of the wave after the bar then determines the strength of shoreline breaking behind the bar. If we assume a monotonically decreasing depth at the shoreline, type (*b*) breaking of Part 1 ($H = \gamma h$) is the most plausible both behind the bar and in the gap. The rate of generation of circulation for vortex [4] is then the difference between the rates of generation of circulation in the gap, and behind the bar. Magnitudes are (see Part 1 for more details)

$$\Gamma_{,t} = \frac{5g\gamma^2}{16}\left[h_B - \left(\frac{\gamma}{\beta}\right)^2 h_c\right] \text{for breaking types } (a) \text{ or } (c) \quad \text{(where } H = \beta h_c \text{ after the bar)}, \tag{A 1}$$

$$\Gamma_{,t} = \frac{5g\gamma^2}{16}(h_B - h_c) \text{ for breaking type } (b) \text{ (where } H = \gamma h_c \text{ after the bar)}. \tag{A 2}$$

Thus, for breaking type (*b*) on the bar, the strength of shore vortex [4] is the same as bar vortex [1]. For breaking types (*a*) and (*c*), the magnitudes in general differ, but remain roughly comparable in magnitude for many typical situations. For narrow gaps, treating the shoreline system as a series of one-dimensional problems may

begin to be inappropriate, as diffraction (decreases strength of vortex [4]) and wave–current interaction (increases strength of vortex [4]) increase in relative importance. Furthermore, if gaps are narrow, wave refraction may defocus energy from the gap thus reducing or possibly even eliminating shore vortex [4]. This may be the case for the narrow rip current topography of MacMahan *et al.* (2005). However, as the width of the gap increases relative to the distance to the shoreline, the presence of a zone of full strength shore break in the gap becomes increasingly certain (as a trivial example, in setup (3)).

Appendix B. Symmetric and antisymmetric track components

Vortex tracks with a mild asymmetry may be separated into symmetric and antisymmetric components. In this paper, the symmetric components are to be compared with the (symmetric) simplified predictions.

At any time, t, vortices [1] and [2] have have known locations, $\boldsymbol{X}_{[1]}$, $\boldsymbol{X}_{[2]}$. The x-location of the symmetric component is taken as the average x-location $x_s = (x_{[1]} + x_{[2]})/2$. The y-locations are taken as half the separation distance from the axis of symmetry, y_c, i.e. $y_{s[1]} = y_c - L/2$, $y_{s[2]} = y_c + L/2$, where $L = |\boldsymbol{X}_{[1]} - \boldsymbol{X}_{[2]}|$.

For the present tests, this should work well in the area of the bar, but becomes less appropriate as asymmetries increase further offshore. All numerical comparisons using this technique are confined to the general area of the bar.

REFERENCES

Abramowitz, M. & Stegun, I. A. 1964 *Handbook of Mathematical Functions*. Dover.

Brocchini, M., Bernetti, R., Mancinelli, A. & Albertini, G. 2001 An efficient solver for nearshore flows based on the WAF method. *Coast. Engng* **43**, 105–129.

Brocchini, M., Kennedy, A. B., Soldini, L. & Mancinelli, A. 2004 Topographically controlled, breaking-wave-induced macrovortices. Part 1. Widely separated breakwaters. *J. Fluid Mech.* **507**, 289–307.

Bühler, O. & Jacobson, T. E. 2001 Wave-driven currents and vortex dynamics on barred beaches. *J. Fluid Mech.* **449**, 313–339.

Chen, Q., Kirby, J., Dalrymple, R., Kennedy, A. & Chawla, A. 2000 Boussinesq modeling of wave transformation, breaking and runup. II: 2D. *J. Waterway, Port, Coastal Ocean Engng* **126**, 48–56.

Chen, Q., Kirby, J., Dalrymple, R., Kennedy, A. & Haller, M. 1999 Boussinesq modelling of a rip current system. *J. Geophys. Res. – Oceans* **104**, 20617–20637.

Haas, K. A. & Svendsen, I. A. 2002 Laboratory measurements of the vertical structure of rip currents. *J. Geophys. Res. – Oceans* **107**, doi:10.1029/2001JC000911.

Haas, K. A., Svendsen, I. A., Haller, M. C. & Zhao, Q. 2003 Quasi-three-dimensional modeling of rip current systems. *J. Geophys. Res. – Oceans* **108**, doi:10.1029/2002JC001355.

Haller, M. C. & Dalrymple, R. A. 2001 Rip current instabilities. *J. Fluid Mech.* **433**, 161–192.

Holland, K. T., Holman, R. A., Lippmann, T. C., Stanley, J. & Plant, N. 1997 Practical use of video imagery in nearshore oceanographic field studies. *IEEE J. Ocean. Engng* **22**, 81–92.

Kennedy, A., Chen, Q., Kirby, J. & Dalrymple, R. 2000 Boussinesq modeling of wave transformation, breaking and runup. I: 1D. *J. Waterway, Port, Coastal Ocean Engng* **126**, 39–47.

Kennedy, A., Chen, Q., Kirby, J. & Dalrymple, R. 2001 Boussinesq-type equations with improved nonlinear performance. *Wave Motion* **33**, 225–243.

Kennedy, A. B. & Thomas, D. A. 2004 Drifter Measurements in a Laboratory Rip Current. *J. Geophys. Res. – Oceans* **109**, doi:10.1029/2003JC001982.

Lamb, H. 1932 *Hydrodynamics*. Dover.

MacMahan, J. H., Thornton, E. B., Stanton, T. P. & Reniers, J. H. M. 2005 RIPEX: Observations of a rip current system. *Mar. Geol.* **218**, 113–134.

Peregrine, D. H. 1998 Surf zone currents. *Theor. Comput. Fluid Dyn.* **10**, 295–309.

Peregrine, D. H. 1999 Large-scale vorticity generation by breakers in shallow and deep water. *Eur. J. Mech.* B/*Fluids* **18**, 403–408.

Piattella, A., Brocchini, M. & Mancinelli, A. 2006 Topographically controlled, breaking-wave-induced macrovortices. Part 3. The mixing features. *J. Fluid Mech.* **559**, 81–106.